Soft Matter

PAPER

Micro- and nanoscale fluid flow on chemical channels†

Fabian Dörfler,[ab] Markus Rauscher,[ab] Joel Koplik,[c] Jens Harting[de] and S. Dietrich*[ab]

We study the time evolution and driven motion of thin liquid films lying on top of chemical patterns on a substrate. Lattice-Boltzmann and molecular dynamics methods are used for simulations of the flow of microscopic and nanoscopic films, respectively. Minimization of the fluid surface area is used to examine the corresponding equilibrium free energy landscapes. The focus is on motion across patterns containing diverging and converging flow junctions, with an eye towards applications to lab-on-a-chip devices. Both open liquid–vapor systems driven by body forces and confined liquid–liquid systems driven by boundary motion are considered. As in earlier studies of flow on a linear chemical channel, we observe continuous motion of a connected liquid film across repeated copies of the pattern, despite the appearance of pearling instabilities of the interface. Provided that the strength of the driving force and the volume of the liquid are not too large, the liquid is confined to the chemical channels and its motion can be directed by small variations in the geometry of the pattern.

1 Introduction

A major theme in recent technological development has been the focus on miniaturization and integration. The prototypical example is the evolution of microelectronic devices for which speed-up and cost reduction complement consumer appeal as the main commercial driving forces for this development. Analogous considerations have spawned the field of microfluidics, *i.e.*, the technology of assembling complex chemical processes into a single miniature laboratory, as a realization of the so-called lab-on-a-chip concept.[1–5] Currently available devices are made of micron-scale structures but further miniaturization down to the nano-scale is expected.[6,7]

The transition from micro- to nano-scale design and fabrication in electronics have required new theoretical ideas in the area of mesoscopic quantum mechanics.[8–10] Pursuing the analogy, nanofluidic developments require as a new element the focus on new aspects of fluid mechanics. At the nano-scale the macroscopic description of fluids in terms of classical hydrodynamic equations breaks down. Boundary layers dominate, thermal fluctuations and hydrodynamic slip become relevant, the range of intermolecular interactions is comparable to the system size, and the finite size of the constituent particles has to be taken into account.[11–15] Although this presents a major challenge for further miniaturization there are many ways in which one can make use of nano-scale specific properties of fluids, *e.g.*, for sorting and sieving of biomolecules. Ion channels in biological membranes and cell walls are another particularly intriguing and inspiring example.[16–23]

Most commercially available fluidic devices consist of closed channels formed by a substrate with grooves covered by a plate. Closed channels offer the advantages of preventing evaporation and of allowing for pumping by applying a pressure difference between the inlet and the outlet. However, clogging is a serious problem and cleaning is difficult. Open microfluidic systems, for which droplets and rivulets are confined to chemical channels formed by hydrophilic surface domains on a hydrophobic or less hydrophilic substrate, have been proposed as a remedy.[24–28] Although one cannot apply a pressure difference between the inlet and the outlet, the flow in chemical channels can be induced by capillary forces, *i.e.*, by wicking into channels[26] or due to wettability gradients,[29] by electrowetting,[30–34] Marangoni forces due to optically,[35,36] electrically,[37,38] or externally generated temperature gradients, (centrifugal) body forces,[39] surface acoustic waves,[40] or shear flow in a covering immiscible fluid,[41] which would also prevent evaporation.

A detailed understanding of equilibrium wetting phenomena on chemically structured substrates is the basis for designing open microfluidic devices. In particular the morphology of nonvolatile fluid droplets on chemical channels has been studied in detail and morphological transitions have been observed. On linear chemical channels one encounters a transition from bulge-shaped droplets for large volumes and large equilibrium contact

aMax-Planck-Institut für Intelligente Systeme, Heisenbergstr. 3, D-70569 Stuttgart, Germany. E-mail: dietrich@is.mpg.de
bInstitut für Theoretische und Angewandte Physik, Universität Stuttgart, Pfaffenwaldring 57, D-70569 Stuttgart, Germany
cBenjamin Levich Institute and Department of Physics, City College of the City University of New York, New York, NY 10031, USA. E-mail: koplik@sci.ccny.cuny.edu
dDepartment of Applied Physics, Technische Universiteit Eindhoven, 5612 AZ Eindhoven, The Netherlands. E-mail: j.d.r.harting@tue.nl
eInstitut für Computerphysik, Universität Stuttgart, Pfaffenwaldring 27, D-70569 Stuttgart, Germany
† Electronic supplementary information (ESI) available. See DOI: 10.1039/c2sm25747e

angles on the channel to elongated rivulets for small volumes and small equilibrium contact angles on the channel.[24,42–45] On ring-shaped structures there is also a droplet state which covers the whole ring.[46,47] This richness in morphological phases is a result of the constant volume constraint for non-volatile fluids. Volatile fluids, which are in chemical equilibrium with their vapor phase, cannot form stable droplets on homogeneous substrates. Accordingly, most of the morphologies on structured substrates, which are stable for non-volatile fluids, turn out to be unstable for volatile fluids: if the pressure in a fluid configuration decreases with increasing volume the drop will either grow without limit or evaporate since the vapor acts as a reservoir with fixed pressure and chemical potential.

However, wetting experiments with volatile fluids are easier to control than those with non-volatile fluids. While in the latter case one must deposit a tiny but well defined amount of fluid on a substrate, in the first case one can tune the pressure in the condensed phase by changing the chemical potential of the reservoir. In addition, transport through the vapor is much faster than along the surface, such that equilibration is much faster and not hindered by pinning of three-phase contact lines. Equilibrium wetting phenomena of volatile fluids on homogeneous substrates are rather well understood:[48,49] the fluid forms a homogeneous wetting film which grows in thickness as the bulk liquid–vapor coexistence line is approached from the gas-side. The wetting behavior of chemically patterned surfaces has been studied in detail[50,51] and the occurrence of morphological wetting transitions from very thin to thicker rivulets has been predicted for linear chemical nano-channels.[52,53] However, only recently it has become possible to manufacture such structures with negligible height difference between the channel and the surrounding substrate.[54,55]

With possible applications as nanofluidic devices in mind, here we discuss the dynamics of quasi-non-volatile droplets (i.e., liquid droplets with a very small vapor pressure) connected by a continuous thin film, both localized on a branched chemical channel pattern. Neither lattice Boltzmann simulations nor molecular dynamics simulations can model systems with truly zero vapor pressure. The pattern has the shape of a ring which is connected periodically to copies of itself. This is the simplest geometry which incorporates the key features of any potential device: one inlet, one outlet, and the splitting and reconnection of distinct fluid paths. This pattern has the further advantage of retaining overall periodicity so that particles need not be added or removed from the system, which greatly simplifies all particle-based calculations. We do not address dewetting on chemical channels, thus putting aside the large body of research on dewetting of thin fluid films on homogeneous and heterogeneous surfaces (see, e.g., ref. 56–62 and references therein).

The paper is organized such that in Section 2 we review the lattice-Boltzmann (LB) method with the focus on its application to simulations of a system with two immiscible fluids. In Section 3 we discuss the shear-cell configuration used in our calculations, in which initially one fluid rests on top of a ring-shaped pattern as a liquid ridge, while the second fluid fills the remaining part of the simulation cell. The applied LB method does not take into account thermal fluctuations. Hence the results reflect ordinary continuum fluid mechanics and most reasonably correspond to microscale rather than nanoscale

systems. The simulations generally show that chemical patterning does successfully direct fluid motion, despite a hydrodynamic instability leading to the appearance of mobile non-uniform bulges or pearls of the fluid which prefers the chemical channels. Furthermore, a control mechanism for influencing fluid motion at a branching out of fluid paths can be inferred from the simulations.

In Section 4 we apply molecular dynamics (MD)[63] as the optimal method for describing nanoscale systems, in order to study the same flow geometry. These calculations resemble earlier ones involving a linear (strip) wetting pattern.[41] We again find that the fluid motion is successfully directed by the pattern. Remarkably, the results also resemble the LB calculations although those cover a much larger length scale, suggesting that chemical patterns provide a very robust means of flow control. Although the multicomponent LB calculations presented here cannot adequately handle a liquid–vapor system, there is no such limitation for MD,[39] and we present several examples of pattern-controlled motion in body force driven systems (this type of driving does not work in the two-fluid case studied in the LB simulations). When body force driven rivulets on sufficiently large patterns are simulated, we find a limitation for flow control: if too much liquid accumulates at a region near a junction, surface tension forces may be overcome by inertia and the liquid may spill off the pattern.

Since surface tension is a dominant force in these systems and because the fluid behavior at the junctions of the patterns is the key for controlling liquid motion, in Section 6 we study the interfacial free energy landscape of a fluid droplet near a junction using the Surface Evolver software package.[64] These results are directly relevant for the body force driven MD simulations because the Lagrange multiplier used to fix the lateral position of the drop corresponds to a lateral force field. Finally, in Section 7 we present conclusions and an outlook on future challenges.

2   The lattice Boltzmann method

The LB method is an indirect solver for the continuum fluid dynamic equations, which mimics the underlying kinetics of the fluid particles on a lattice in real space with a discrete set of velocity degrees of freedom. This method is attractive for the current application because a number of multiphase and multi-component models exist which are comparably straightforward to implement[65–71] and because it has been used to simulate the dynamics of drops on chemically patterned substrates.[72,73] In the following, the LB model used here is described briefly in order to introduce the parameters which are crucial for the fluid dynamic description. A detailed discussion of the model can be found in the references cited below.

We use a three-dimensional implementation of the multi-component Shan–Chen model (SCM)[65,66,74–77] with a so-called D3Q19-lattice,[78] i.e., a three-dimensional cubic lattice in real space with a lattice constant a and a set of 19 velocity degrees of freedom c_α, $\alpha \in \{1,...,19\}$, at any lattice site with a position vector r (see Fig. 1). The state of the system at a certain time t is given by a set of dimensionless distributions $f_\alpha^s(r,t)$, which upon normalization give the fraction of particles of species s at a site r with the velocity degree of freedom c_α, i.e., $N^s = \sum_{\{r\}} \sum_\alpha f_\alpha^s(r,t)$ is the total number of s-type particles within the system. Resting

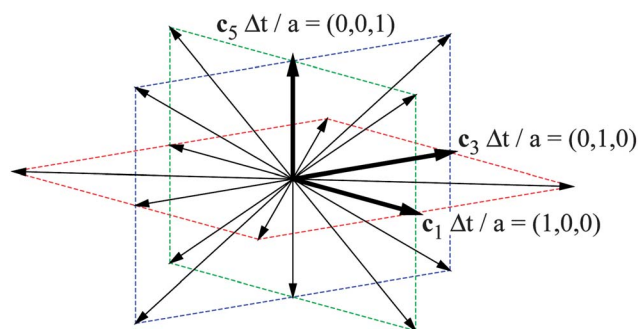**Fig. 1** The structure of the $D3Q19$-lattice. Starting from the central site $\boldsymbol{r}$ the velocities $\{\boldsymbol{c}_1,\ldots,\boldsymbol{c}_{18}\}$ allow particle transport to the neighboring sites located in the planes (indicated by color) normal to the $\boldsymbol{c}_1$, the $\boldsymbol{c}_3$, and the $\boldsymbol{c}_5$ direction (dash-dotted vectors). $\boldsymbol{c}_{19} = (0,0,0)$ corresponds to particles resting at $\boldsymbol{r}$. Upon normalization by means of the lattice constant a and the time step Δt, the vectors $\boldsymbol{c}_1$, $\boldsymbol{c}_3$, and $\boldsymbol{c}_5$ form a local, right handed, orthonormal basis so that $\boldsymbol{r}_\alpha = \boldsymbol{r} + \boldsymbol{c}_\alpha \Delta t$ renders the lattice sites in real space.

fluid particles are taken into account by non-zero values of $f_{19}^s(\boldsymbol{r},t)$ with $\boldsymbol{c}_{19} \equiv (0,0,0)$, whereas $|\boldsymbol{c}_{\alpha \neq 19}| \neq 0$. The particle masses m^s do not play a physical role in the following, thus we set $m^s \equiv m \; \forall s$, i.e., all particles of all species s have a unit mass m.

With our implementation of the SCM, the temporal evolution of the distributions $f_\alpha^s(\boldsymbol{r},t)$ follows the scheme

$$\frac{f_\alpha^s(\boldsymbol{r} + \boldsymbol{c}_\alpha \Delta t, t + \Delta t) - f_\alpha^s(\boldsymbol{r},t)}{\Delta t} = -\frac{1}{\lambda^s}\left[f_\alpha^s(\boldsymbol{r},t)\right.$$
$$\left. -\phi^s\left(\left|\boldsymbol{c}_\alpha - \bar{\boldsymbol{u}}^s(\boldsymbol{r},t)\right|^2\right)\right], \quad (1)$$

where $\boldsymbol{r}$ and $\boldsymbol{r} + \boldsymbol{c}_{\alpha \neq 19}\Delta t$ refer to neighboring lattice sites, i.e., off-lattice particle positions do not occur. The left hand side of eqn (1) provides the convection of f_α^s on the lattice along the direction of $\boldsymbol{c}_\alpha$ per time unit Δt, and the right hand side effectively models a local relaxation of f_α^s towards a dimensionless local Maxwellian velocity distribution ϕ^s with a relaxation time scale λ^s. The Maxwellian distribution ϕ^s is centered in velocity space around the velocity $\bar{\boldsymbol{u}}^s$ (to be defined below) and its width $c_T = \sqrt{k_B T/m}$ is proportional to the thermal velocity. Upon associating the internal energy per particle $\frac{3}{2}k_B T$ with the kinetic energy $\frac{m}{2}(a/\Delta t)^2$ one obtains

$$c_T = \sqrt{\frac{k_B T}{m}} = \frac{1}{\sqrt{3}}\frac{a}{\Delta t}, \quad (2)$$

which implies $T \propto m k_B^{-1}(a/\Delta t)^2$, so that by construction the SCM is isothermal[79,80] with the temperature T fixed by the unit particle mass m, the time step Δt, and the lattice constant a.

The zeroth moment of the distributions $f_\alpha^s(\boldsymbol{r},t)$ leads directly to the local number density of species s,

$$\rho^s(\boldsymbol{r},t) = \frac{n^s(\boldsymbol{r},t)}{a^3} = \frac{1}{a^3}\sum_\alpha f_\alpha^s(\boldsymbol{r},t), \quad (3a)$$

where $n^s(\boldsymbol{r},t) = \sum_\alpha f_\alpha^s(\boldsymbol{r},t)$ renders the number of particles of species s at the site $\boldsymbol{r}$. The local velocity field $\boldsymbol{u}^s(\boldsymbol{r},t)$ for species s is defined by the first velocity moment and the so-called Shan–Chen acceleration $\boldsymbol{F}^s$,

$$\boldsymbol{u}^s(\boldsymbol{r},t) = \frac{1}{n^s}\left(\sum_\alpha \boldsymbol{c}_\alpha f_\alpha^s + \frac{1}{2}\boldsymbol{F}^s \Delta t\right). \quad (3b)$$

The last term is needed in order to compensate for discretization artefacts and to obtain Navier–Stokes equations on the fluid dynamic level.[76] The corresponding total quantities are given by a summation over all types: $\rho(\boldsymbol{r},t) = \sum_s \rho^s$ and $\boldsymbol{u}(\boldsymbol{r},\text{t}) = \rho^{-1}\sum_s \rho^s \boldsymbol{u}^s$. The key feature of the SCM is the acceleration[65]

$$\boldsymbol{F}^s(\boldsymbol{r},t) = -\psi^s(\boldsymbol{r},t)\sum_{\{\tilde{s}\}}\mathscr{G}^{s\tilde{s}}\sum_{\tilde{\alpha}}\psi^{\tilde{s}}\left(\boldsymbol{r} + \boldsymbol{c}_{\tilde{\alpha}}\Delta t, t\right)\boldsymbol{c}_{\tilde{\alpha}}\Delta t, \quad (4)$$

which is often interpreted as the local effective acceleration of a particle of type s at the lattice site $\boldsymbol{r}$ due to the presence of particles at the neighboring sites $\boldsymbol{r} + \boldsymbol{c}_{\tilde{\alpha}}\Delta t$. The coupling strength $\mathscr{G}^{s\tilde{s}}$ defines attraction (negative sign of $\mathscr{G}^{s\tilde{s}}$) or repulsion (positive sign of $\mathscr{G}^{s\tilde{s}}$) between two particles of type s and of type $\tilde{s}$. The so-called pseudo density $\psi^s(\boldsymbol{r},t) = 1 - \exp[-n^s(\boldsymbol{r},t)]$ is determined by the local partial particle number $n^s(\boldsymbol{r},t)$. The acceleration $\boldsymbol{F}^s$ enters the evolution scheme given by eqn (1) via the velocity $\bar{\boldsymbol{u}}^s$, which determines the center of the Maxwellian distribution ϕ^s in velocity space,

$$\bar{\boldsymbol{u}}^s(\boldsymbol{r},t) = \boldsymbol{u}^s + \frac{\boldsymbol{F}^s}{n^s}\lambda^s = \frac{1}{n^s}\left[\sum_\alpha \boldsymbol{c}_\alpha f_\alpha^s + \left(\frac{1}{2}\Delta t + \lambda^s\right)\boldsymbol{F}^s\right]. \quad (5)$$

The expressions for $\boldsymbol{u}^s$, $\boldsymbol{F}^s$, and $\bar{\boldsymbol{u}}^s$ given by eqn (3b), (4), and (5), respectively, are constructed such that in the large scale limit one obtains fluid dynamic equations with a non-ideal equation of state. (In the case of a one-component system for a negative sign of $\mathscr{G}^{ss}$, i.e., attraction among particles of the same species, the pseudo density ψ^s as given above leads to a van-der-Waals loop.) One can show that this approach is equivalent to treating the acceleration $\boldsymbol{F}^s$ formally as an external field.

In the simulations, we minimalistically mimic the kinetics of a system consisting of an o-type fluid (oil) covering a w-type fluid (water) rivulet so that each fluid is in contact with certain parts of an r-type substrate (rock, or more generally, solid). The model is minimalistic in the sense that oil and water particles are distinguished by a repulsive interaction only, i.e., $\mathscr{G}^{ow} > 0$ with equal relaxation time scales for both oil and water, $\lambda^o = \lambda^w \equiv \lambda$. The rock particles are pinned to their lattice sites, i.e., $f_{19}^r(\boldsymbol{r},t) \equiv$ constant and $f_{\alpha \neq 19}^r(\boldsymbol{r},t) \equiv 0$ for all times t, respectively. Together with bounce back boundary conditions this effectively results in a hydrophobic solid boundary if $f_{19}^r > 0$ and $\mathscr{G}^{rw} > 0$.

In order to induce oil–water phase separation and thus to facilitate wetting, our choice for the coupling constants $\mathscr{G}^{s\tilde{s}}$ is

$$\mathscr{G}^{oo} = \mathscr{G}^{ww} = \mathscr{G}^{or} \equiv 0, \quad \mathscr{G}^{ow} = \mathscr{G}^{rw} \equiv \mathscr{G} > 0. \quad (6)$$

The phase separation of oil and water is driven by the parameter $\mathscr{G}$, and the wetting behavior for a given $\mathscr{G}$ depends on the local, partial number densities of oil, water, and rock particles, ρ^o, ρ^w, and ρ^r, respectively. With this choice of parameters, phase separation is almost complete and the concentration of oil in the water phase and vice versa is negligible (smaller than 0.2% in weight).

2.1 The fluid dynamic level

In the strong segregation limit, within the water or the oil phase the fluid dynamic equations for the majority species $s \in \{o,w\}$,

i.e., for the quantities ρ^s and u^s defined by eqn (3a) and (3b), respectively, can be obtained *via* a systematic Chapman–Enskog analysis of eqn (1).[67,76,79,81] With $\partial_t = \partial/\partial t$, $\partial_i = (\nabla)_i$ and $u_i^s = (u^s)_i$ for $i = 1, 2, 3$, and upon neglecting terms of $\mathcal{O}((u^s/c_T)^{k>2})$, *i.e.*, within the regime of sufficiently small Mach numbers $(u^s/c_T)^2$, the continuity equation is

$$\partial_t\rho^s + \partial_i(\rho^s u_i^s) = 0, \tag{7a}$$

and the balance of momentum reads

$$m\rho^s(\partial_t + u_j^s\partial_j)u_i^s \approx -\partial_j p^s\delta_{ij} + \partial_j\eta^s(\partial_j u_i^s + \partial_i u_j^s). \tag{7b}$$

In other words the lattice Boltzmann dynamics solves the Navier Stokes equations for fluids of viscosity η^s; p^s is the partial pressure of species s. In the limit of nearly complete phase separation, the density of the minority phase is negligible and therefore it does not contribute to the momentum balance. These are the compressible Navier–Stokes equations, which imply number conservation and conservation of the total momentum as the sum of all momenta of all particles (upon $(u^s/c_T)^2 \to 0$ the incompressible regime is approached asymptotically because the Chapman–Enskog analysis renders both $\nabla\rho$ and $\nabla\cdot u^s$ to be of $\mathcal{O}((u^s/c_T)^2)$).

For a single component and single phase system the local pressure can be calculated using the equation of state $p = mc_T^2\rho = k_B T\rho$ of an ideal gas. However, for a binary mixture and for the choice of parameters given in eqn (6) non-ideal contributions to the pressure come into play and one obtains

$$\frac{p}{mc_T^2} = \rho^o + \rho^w + \frac{(\Delta t)^2}{a^3}\sum_{s,\bar{s}\in\{o,w\}}\mathscr{G}^{s\bar{s}}\psi^s\psi^{\bar{s}}. \tag{8}$$

With the choices given by eqn (6) and a coupling parameter $\mathscr{G}$ strong enough to induce nearly complete oil–water phase separation, the partial pressure of the minority species is negligible. The partial pressure of the majority species s in the homogeneous s-phase resembles that of an ideal gas,

$$p^s = \rho^s k_B T, \tag{9}$$

because a vanishing pseudo density $\psi^{\bar{s}}$ of the minority species $\bar{s}$ renders the non-ideal part in eqn (8) negligible. Non-ideal behavior appears only within the interfacial region separating the two distinct homogeneous phases (with majority species w and o, respectively), where the Chapman–Enskog analysis is not applicable. This implies that interfacial tensions and contact angles have to be determined from simulation results. At present there are no explicit formulae which allow one to calculate them directly from the simulation parameters.

In a nearly complete phase separated system the shear viscosity in the homogeneous s-phase reads

$$\eta \approx \eta^s = m\rho^s c_T^2\left(\tau - \frac{1}{2}\right)\Delta t \tag{10}$$

with the dimensionless relaxation time $\tau = \lambda/\Delta t$. We note that, first, η^s depends linearly on the local number density ρ^s, which is a property of dilute fluids, second, that η^s changes upon varying the timestep Δt, and third, that η^s does not depend on the coupling parameters $\mathscr{G}^{s\bar{s}}$ (because in eqn (6) the self-coupling is set to zero).

3 Lattice Boltzmann simulations

The chemical pattern is implemented *via* a lateral variation of the fixed rock density ρ^r leading to channel-like hydrophilic surface domains with a certain width w embedded in a hydrophobic substrate with contact angles $\theta_{phil} < 90°$ and $\theta_{phob} \approx 140°$, respectively. (The contact angle is defined as the angle of the oil–water interface at a homogeneous rock surface for a macroscopically large water droplet.) We have investigated two types of patterns: a symmetric pattern with *xz*-mirror symmetry, and an asymmetric pattern with broken *xz*-mirror symmetry (see Fig. 2(a)). The simulation box is designed as a shear cell, which means that a no-slip boundary condition is imposed at the substrate, both lateral boundary conditions are periodic, and a constant flow velocity aligned parallel to the *x*-direction is imposed within the top layer of lattice sites in the simulation box, *i.e.*, $u^{o,w}(r,t)|_{toplayer} \equiv (v_{shear},0,0)$.

For both the symmetric and the asymmetric pattern, we have run simulations for two different hydrophilic contact angles,

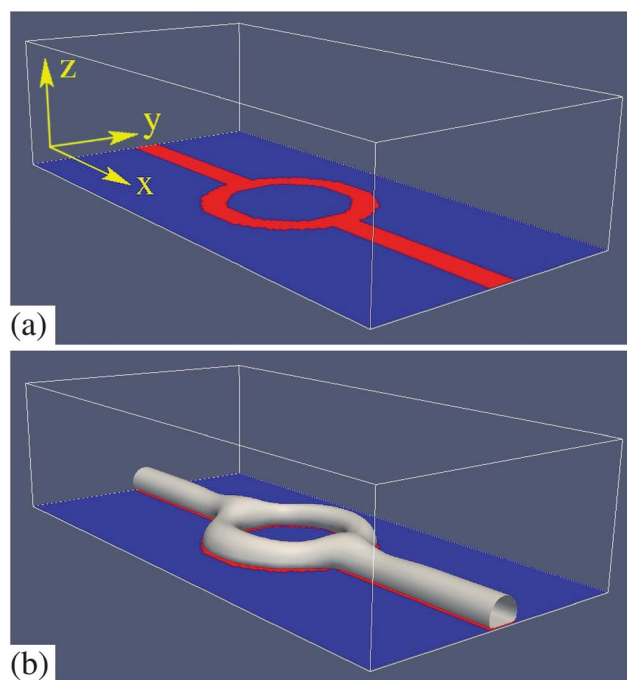**Fig. 2** (a) We have used a simulation box with dimensions $128a \times 64a \times 32a$ in the *x*-, *y*-, and *z*-direction and with the substrate in the *xy*-plane as the bottom wall. The chemical pattern provides hydrophilic areas, marked in red, embedded in a hydrophobic substrate, marked in blue. The clipping of hydrophilic and hydrophobic domains is sharp, *i.e.*, the transition between the red and the blue domains occurs within one lattice spacing a. In the symmetric case all the hydrophilic sections have a uniform width $w = 6a$, and the outer radius of the ring is $20a$. In the asymmetric case the outer radius of the front branch (the branch with smaller values of y) is narrowed by one a. The pattern junctions are termed the upstream and the downstream junction with respect to the direction of the shear velocity $u^{o,w}|_{top\ layer}=(v_{shear} \geq 0,0,0)$ in the *x*-direction. (b) Morphology of a water rivulet on a symmetric pattern at early stages ($100\,\Delta t$) for $\theta_{phil} \approx 80°$, $\theta_{phob} \approx 140°$, and $v_{shear}/c_T \approx 0.12$, displayed as the isosurface $\mathscr{A}$ of half the density in bulk water. For a description of the initial configuration ($t = 0$) see the main text. The onset of the pearling instability is already visible in the form of small bulges above the pattern junctions.

$\theta_{\text{phil}} \approx 30°$ and $\theta_{\text{phil}} \approx 80°$, and for two different shear velocities, $v_{\text{shear}}/c_T = 0.12$ and $v_{\text{shear}}/c_T = 0.17$. The initial fluid geometry is given by a water rivulet covering the pattern with a square cross-section $w \times w$ and the rest of the simulation box filled with oil, *i.e.*, for the box dimensions given in Fig. 2 one has $V/w^3 \approx 32$ for the water volume V. Both water and oil have homogeneous initial number densities, $\rho^{\text{o,w}} = \rho = 0.7a^{-3}$, and the spatial variation of the densities between the water and the oil phases occurs within one lattice spacing a. The coupling strength within the acceleration $\boldsymbol{F}^{\text{s}}$ (eqn (4)) is $\mathscr{G} = 0.20/\lambda^2$ and the dimensionless relaxation time is $\tau = \lambda/\Delta t = 1.0$, which leads to an oil–water surface tension[82] $\gamma \approx 0.07m/\lambda^2$ and a shear viscosity $\eta^{\text{o,w}} = m\rho c_T^2 \lambda/2$ for both oil and water (see eqn (2) and (10) for $\tau = 1$).

With $\tau = 1$ the Reynolds number and the capillary number for the water rivulet are $\text{Re} = m\rho^{\text{w}} w v_{\text{shear}}/\eta^{\text{w}} = \sqrt{12}(w/a)(v_{\text{shear}}/c_T)$ and $\text{Ca} = \eta^{\text{w}} v_{\text{shear}}/\gamma = [(c_T\lambda)^3 \rho^{\text{w}}/(2\gamma\lambda^2)](v_{\text{shear}}/c_T) = [m\rho^{\text{w}} a^3/(\sqrt{108}\gamma\lambda^2)](v_{\text{shear}}/c_T)$, *i.e.*, due to $\tau = 1.0$ and $w/a = 6$,

$$\text{Re} \approx 20.8 \frac{v_{\text{shear}}}{c_T}, \quad \text{Ca} \approx 0.96 \frac{v_{\text{shear}}}{c_T}. \quad (11)$$

According to our choices given above, the ratio v_{shear}/c_T is of $\mathscr{O}(10^{-1})$, so that Re is of $\mathscr{O}(10^0)$ and Ca is of $\mathscr{O}(10^{-1})$. This means that we have laminar flow with a strong influence of the surface tension on the evolution of the oil–water interface. The temporal evolution of the system is followed by monitoring the isosurface of the water density corresponding to half its bulk value.

3.1 General features

The initially square-shaped water ridges evolve very fast (within less than $100\,\Delta t$) towards a circular cross-sectional shape. Oil and water are separated into coexisting thermodynamic bulk phases, *i.e.*, there is an oil bulk phase with a very low density of water particles (smaller than 0.2% in weight) and *vice versa*. The oil–water interface has a well-defined width of about $4a$ (see Fig. 2(b) and 3). The water and oil bulk densities are somewhat above the initial values: $\rho^{\text{w}} \approx 0.84a^{-3}$ and $\rho^{\text{o}} \approx 0.74a^{-3}$ compared to the initial values $\rho^{\text{w}} = \rho^{\text{o}} = 0.7a^{-3}$. This is a consequence of the Laplace pressure (recall eqn (9)) in combination with the finite volumes of the emerging interfacial regions.

The water ridges are unstable with respect to pearling,[39] *i.e.*, they are subject to a surface tension driven instability which leads to a breakup into droplets, whereupon the dynamics of the pearling process for a given non-zero shear velocity v_{shear} is controlled by the values of Ca and θ_{phil} is driven by the oil–water surface tension and is hindered by viscosity and the attractive fluid–substrate interactions, which means that the pearls preferentially form at the pattern junctions and the pearling is slower and less pronounced for the case $\theta_{\text{phil}} \approx 30°$ compared to the case $\theta_{\text{phil}} \approx 80°$. Due to compressibility (recall eqn (7)), the water density in the interior decreases with a decreasing mean curvature of the oil–water interface, *i.e.*, $\rho^{\text{w}} < 0.8a^{-3}$ inside big droplets enclosing the vast majority of water in the system and $\rho^{\text{w}} < 0.9a^{-3}$ inside very small droplets.

3.2 $\theta_{\text{phil}} \approx 80°$

Fig. 4 shows the time evolution for $v_{\text{shear}}/c_T = 0.12$ and $\theta_{\text{phil}} \approx 80°$. At early times, the water transport due to pearling dominates over the transport due to shear flow. This means that whole
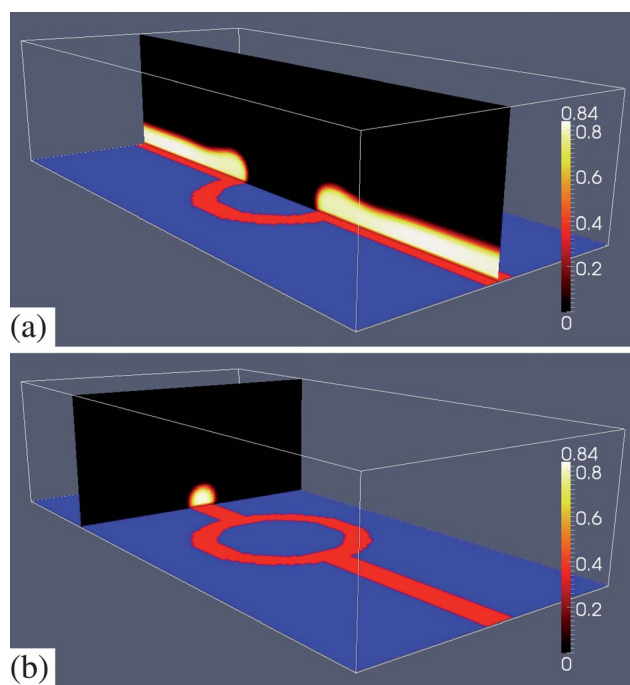

Fig. 3 Cuts of the density profile of the configuration shown in Fig. 2(b), along (a) and perpendicular to (b) the xz-symmetry plane. The color code refers to the water density ρ^{w} in units of a^{-3} with a bulk value (*i.e.*, in the interior of the rivulet) of $\rho^{\text{w}} \approx 0.84a^{-3}$. The water density drops from the bulk value to almost zero within a range of about $4a$. The same holds for the oil density; however, the bulk value of the oil density (*i.e.*, far from the substrate) is $\rho^{\text{o}} \approx 0.74a^{-3}$, $\theta_{\text{phil}} \approx 80°$ and $\theta_{\text{phob}} \approx 140°$.

water droplets move along the wetting pattern in tandem with their formation by the pearling process. The figure appears to show isolated droplets separated by a waterfree substrate, but this is an artifact of the plotting procedure. In fact, a layer of water with about one to two a in thickness and with approximately 1% of the water bulk density is permanently adsorbed at the pattern. As will be discussed in Section 5, a is on the order of 50 nm. Therefore the aforementioned amount of water adsorbed on the chemical channels is an artifact of the mesoscopic width of the diffused interface. This will influence (most likely facilitate) the motion of the three-phase contact line. However, we do not expect that this aspect qualitatively influences our results.

Density fluctuation due to numerical round-off errors influences the fluid behavior at the symmetric upstream junction, *i.e.*, the droplets randomly choose one of the two branches to move downstream. At an asymmetric upstream junction, due to surface tension forces the wider rear branch is preferred. Bigger droplets sample more of the linear shear flow profile and therefore are driven faster than smaller ones.

Fig. 5 shows the fluid behavior for the higher shear rate $v_{\text{shear}}/c_T = 0.17$. In the symmetric case, at this rate big droplets are finally driven off the pattern at the upstream junction, whereas the big final droplet is still guided by the pattern in the asymmetric case, yet with a significant spillage onto the hydrophobic domain ($\theta_{\text{phob}} \approx 140°$). Due to the enhanced shear drive, tails grow out of the moving droplet, which eventually break up into pearls (this phenomenon might be related to the formation of Landau–Levich films in coating problems).
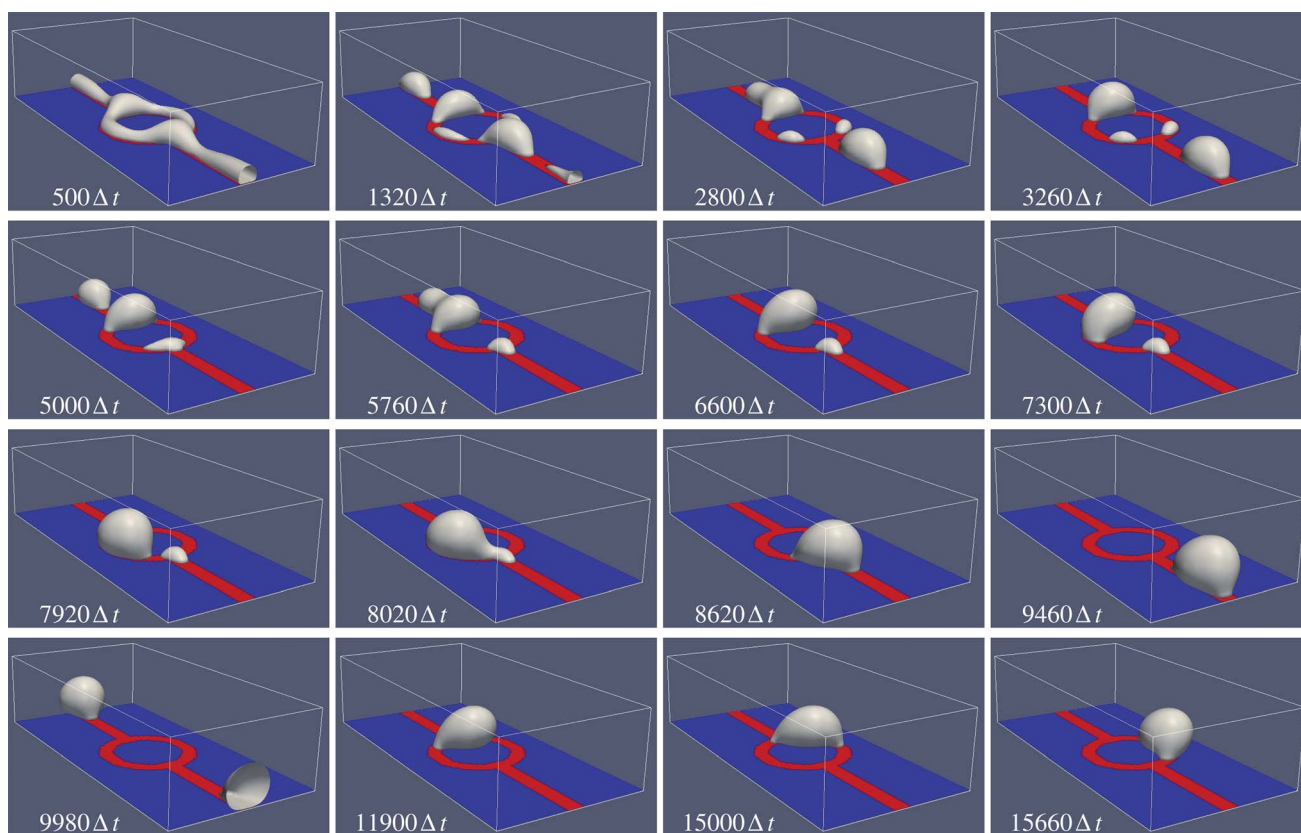
Fig. 4 Simulation snapshots for $\theta_{phil} \approx 80°$, $\theta_{phob} \approx 140°$, and $v_{shear}/c_T \approx 0.12$ on a symmetric pattern. The pictures are arranged in consecutive rows with the flow of time from left to right. The pearling at early times, the aggregation and merger of droplets at the junctions, as well as the random droplet behavior at the upstream junction (*i.e.*, whether turning right or left) can be seen. The randomness is introduced by numerical round-off errors in the simulation code. Note the periodic boundary conditions in the *x*-direction. For a movie see the file *symm_80deg_lowshearLB.avi*.

For additional illustration see the movie files *symm_80deg_lowshearLB.avi*, *symm_80deg_highshearLB.avi*, and *asymm_80deg_highshearLB.avi* corresponding to Fig. 4, 5(a) and (b), respectively. For a movie corresponding to the simulation parameters in Fig. 5 but on an asymmetric pattern see the file *asymm_80deg_lowshearLB.avi*.

3.3 $\theta_{phil} \approx 30°$

Fig. 6(a) and (b) show the results for the shear rate $v_{shear}/c_T = 0.12$. On the symmetric pattern, a single droplet gets stuck permanently at the upstream junction, whereas there is no permanent hang up on the asymmetric pattern. The enhanced water–rock interaction leads to a water coating of the channel
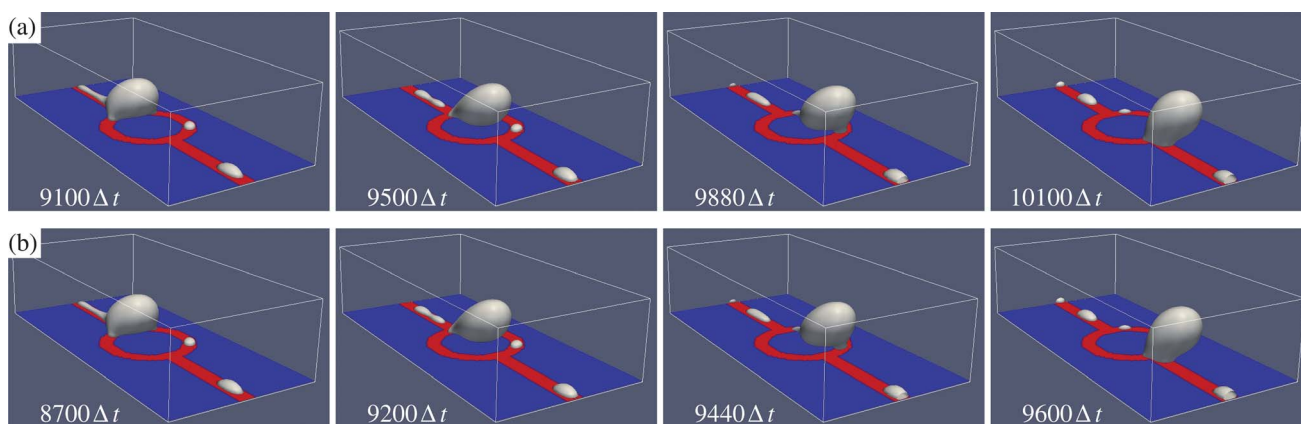

Fig. 5 Simulation snapshots for $\theta_{phil} \approx 80°$, $\theta_{phob} \approx 140°$, and $v_{shear}/c_T = 0.17$ on a symmetric (a) and an asymmetric pattern (b). In the symmetric case the droplet is driven off the pattern, whereas in the asymmetric case it is still guided by the wider rear branch of the pattern. For a movie see the files *symm_80deg_highshearLB.avi* and *asymm_80deg_highshearLB.avi* for (a) and (b), respectively.

sections the droplet has run over, *i.e.*, a water coverage far beyond the minimal adsorption mentioned above.

For the higher shear rate $v_{\text{shear}}/c_T = 0.17$ Fig. 6(c) shows that no permanent hang up occurs at a symmetric upstream junction. Instead, numerical round-off errors influence the fluid behavior as already described for $\theta_{\text{phil}} \approx 80°$ and $v_{\text{shear}}/c_T = 0.12$. However, after the first passage the xz-mirror symmetry of the system remains broken by an unequal water coating, and hence the droplet path is predetermined for any consecutive passage by the film left behind the droplet. In the asymmetric case, the situation is qualitatively the same as the one above for $v_{\text{shear}}/c_T = 0.12$.

For additional illustration see the movie files *symm_30deg_lowshearLB.avi*, *asymm_30deg_lowshearLB.avi*, and *symm_30deg_hightshearLB.avi* corresponding to Fig. 6(a)–(c), respectively. For a movie corresponding to the simulation parameters in Fig. 6(c) but on an asymmetric pattern see the file *asymm_30deg_highshearLB.avi*.

3.4 Flow control options

The upstream junction where the inlet channel branches out in flow direction turns out to be the crucial component of the

pattern, because – provided that the surface tension forces are strong enough to keep the droplet on the pattern – the droplet behavior is determined by symmetry. Droplets get stuck at a symmetric junction since the mirror symmetry of the pattern naturally translates into a mirror symmetry of the droplet morphology, and a splitting of the droplet into two smaller ones is prevented by surface tension. In contrast, surface tension forces drive the droplets onto the wider rear branch of an asymmetric junction.

This might be exploited in order to direct fluid motion and control droplet throughput in potential microfluidic devices: a droplet typically running on the wider rear branch of the asymmetric pattern could be occasionally forced to take the front branch by means of a time-dependent, local variation of the wettability near the junction generated, *e.g.*, by electric pulses or heating.

4 Molecular dynamics simulations

4.1 Methods

The MD simulations involve generic viscous fluids and a crystalline solid substrate constructed of atoms interacting *via*
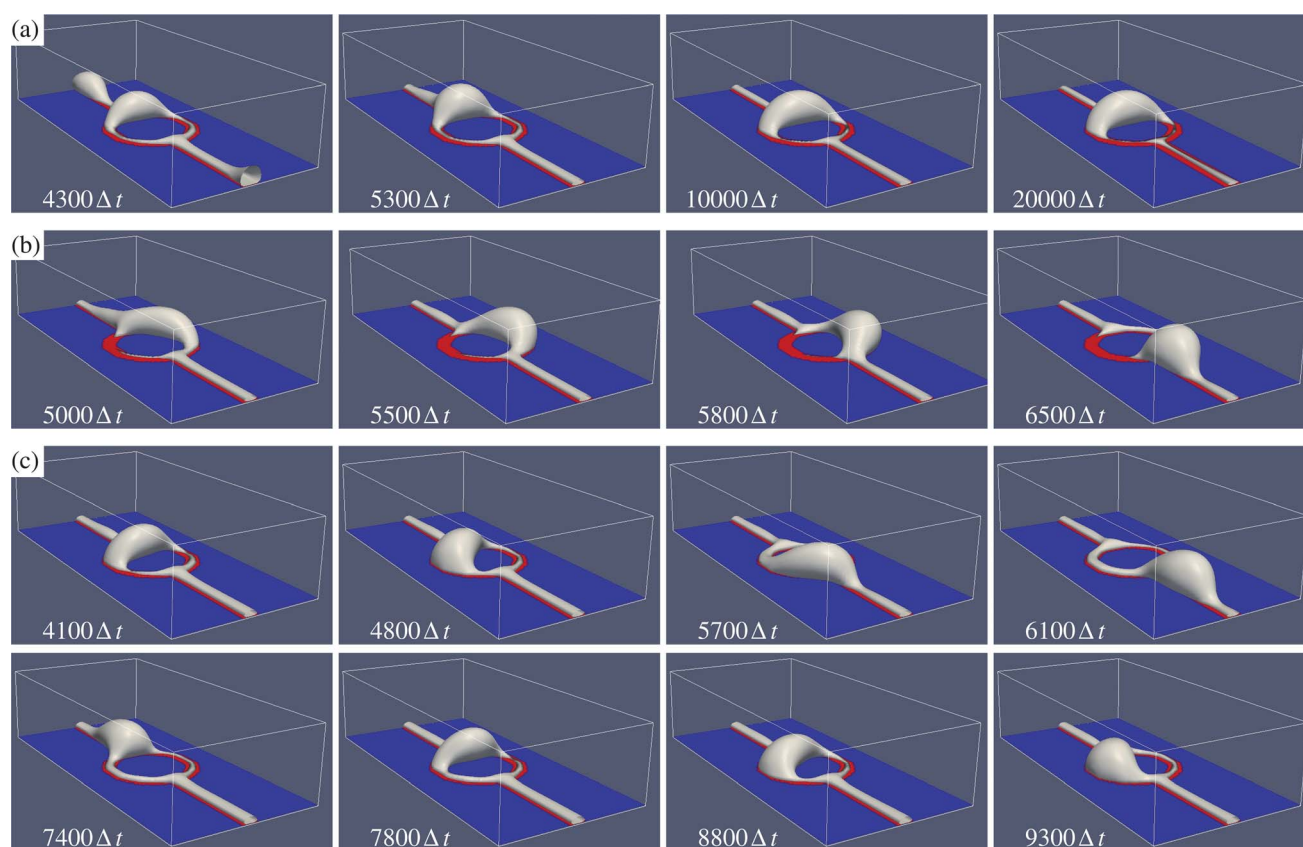

Fig. 6 Simulation snapshots for $\theta_{\text{phil}} \approx 30°$, $\theta_{\text{phob}} \approx 140°$, and $v_{\text{shear}}/c_T \approx 0.12$ on a symmetric (a) and an asymmetric pattern (b). While the droplet gets stuck permanently at the symmetric upstream junction there is no hang up in the asymmetric case. Due to surface tension, the droplet favors the wider rear branch. (c) Simulation snapshots for $\theta_{\text{phil}} \approx 30°$ and $v_{\text{shear}}/c_T \approx 0.17$ on a symmetric pattern. The droplet at the upstream junction randomly chooses one of the branches. Due to the periodic boundary conditions it always takes, however, the same path in any consecutive passage because the mirror symmetry of the system remains broken by an unequal coating of the pattern by water. The droplet leaves behind a significant amount of water on the channel. For a movie see the files *symm_30deg_lowshearLB.avi*, *asymm_30deg_lowshearLB.avi*, and *symm_30deg_hightshearLB.avi* for (a), (b), and (c), respectively.

Lennard-Jones potentials. The shape of the wetting pattern on the solid is similar to the pattern used above for the LB simulations and the computational method is identical to that used in two previous papers. The case of immiscible binary liquid mixtures in a shear cell follows ref. 41, while related calculations involving an open geometry with a liquid ridge of a one-component fluid in contact with its vapor are based on ref. 39. The pair potentials are of the Lennard-Jones form,

$$\Phi_{LJ}(\boldsymbol{r}) = 4\varepsilon \left[\left(\frac{\boldsymbol{r}}{\sigma} \right)^{-12} - c_{s\tilde{s}} \left(\frac{\boldsymbol{r}}{\sigma} \right)^{-6} \right] \quad (12)$$

with the atomic core size σ and the potential depth ε as the characteristic scales of length and energy, respectively. The fluid atoms of all species have the common mass m, so that $t_0 = \sigma\sqrt{m/\varepsilon}$ gives a characteristic time scale. The interaction is cut off at $\boldsymbol{r}_c = 2.5\sigma$ and shifted by a linear term so that the force vanishes smoothly there. The coefficient $c_{s\tilde{s}}$ is used to vary the strength of the attractive interaction between atomic species s and $\tilde{s}$.

In the shear cell case the interaction strength coefficients have the standard value 1.0, except that $c_{s\tilde{s}} = 0$ if s and $\tilde{s}$ refer to atoms of different liquids, or of the inner liquid (the "water") and of the regions outside the pattern, or of the outer liquid (the "oil") and of the regions of the pattern. With this, the two liquids are de facto immiscible and the inner liquid wets the pattern completely ($\theta_{phil} = 0°$), while the regions outside the pattern are completely nonwetting ($\theta_{phob} = 180°$).

In the open case with a one-component fluid, the liquid–liquid and the solid–solid interaction strength coefficients are 1.0, and the liquid–solid coefficients are 1.0 for solid atoms within the pattern (leading to a contact angle $\theta_{phil} = 0°$) and either 0 ("nonwetting", $\theta_{phob} = 180°$) or 0.75 ("partial wetting", $\theta_{phob} \approx 90°$) for the solid atoms outside the pattern. In this open case the liquid consists actually of linear chains of four atoms each, joined by nonlinear (FENE) springs, so as to reduce the vapor pressure and to provide a reasonably sharp interface.

The atoms of the solid substrate are not free, but are tethered to lattice sites by a stiff linear spring with the force law $\boldsymbol{f} = -k(\boldsymbol{r} - \boldsymbol{r}_0)$, where $k = 100\varepsilon/\sigma^2$ and $\boldsymbol{r}$ and $\boldsymbol{r}_0$ are the position of a wall atom and of its lattice position, respectively. The wall atoms have a mass $m_w = 100m$ so that the characteristic frequency $\sqrt{k/m_w} = 1/\tilde{t}_0$ of the wall atom motion is less than that of dimer harmonic oscillations about the LJ potential minimum, which is approximately $7.6/\tilde{t}_0$.

In the shear cell case, the simulation involves 120 040 "water" atoms, 1 799 960 "oil" atoms and 154 880 substrate atoms, in a box of dimensions $273.6\sigma \times 171.0\sigma$ in the substrate plane, with a height of 54.72σ. The width of the wetting strip is 17.1σ and the outer radius of the circular arc is 68.4σ.

The number of fluid atoms in the open flow case shown in Fig. 8 is 119 840 and the number of substrate atoms is 84 480. The box dimensions are identical to those in the shear flow case. With 269 040 fluid and 345 600 substrate atoms and box dimensions of $373.1\sigma \times 559.6\sigma \times 53.0\sigma$ the simulations leading to Fig. 9 and 10 are roughly twice as large.

The simulations are conducted in a box with periodic boundary conditions in all three directions. This implies that in the open case, the molecules in the gas phase hit the bottom of the

substrate. In the case of the shear cell there is an additional top wall which confines the fluid. The final liquid temperature is fixed at $T = \varepsilon/k_B$ by a Nosé–Hoover thermostat. Initially, all atoms are placed on the sites of a *fcc* lattice, with the liquid on top of the wetting region having a rectangular cross-section; the temperature is ramped up to the above final value, allowing the inner liquid to assume a circular cross-sectional shape while remaining on top of the pattern. Without driving, the liquid forms pearls at the nodes of the junction pattern, due to the same surface tension instability as observed in the LB case. However, in the simulations discussed below a driving force is applied before the pearls develop. In the shear-cell case, we translate the atoms in the top wall at constant velocity $0.3\sigma/t_0$, while in the open case a body force of magnitude $0.001 \times m\sigma/t_0^2$ is applied to each atom parallel to the long x-direction of the substrate.

4.2 Shear-cell flow

The results of a simulation in rough correspondence to the LB calculations are shown in Fig. 7. The figure shows snapshots of the interface between two immiscible fluids in a shear cell, defined here as the surface on which the number density of the inner fluid is $0.4\sigma^{-3}$, *i.e.*, roughly half the bulk density of the inner fluid at the same temperature. The dimensions of the wetting pattern and of the initial volume of the inner fluid relative to the volume of the simulation box are in similar proportions to those in the symmetric LB case in Fig. 2(a). Using the definitions for the Reynolds number and the Capillary number in Section 3.1, we have Re $\approx$ 0.21 and Ca $\approx$ 0.56 (compared to $2.5 \lesssim$ Re $\lesssim 3.5$ and $0.12 \lesssim$ Ca $\lesssim 0.16$ in the LB simulations, see also Section 5 for a discussion). The corresponding values for the viscosity of the inner liquid and for the liquid–liquid surface tension are $\eta^w \approx 2.12m/(\sigma t_0)$ (obtained from a separate simulation of
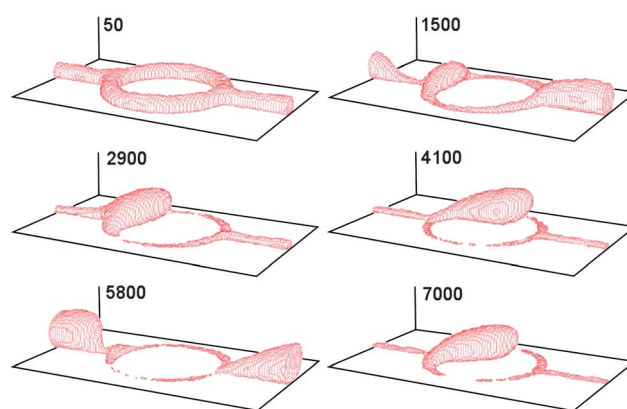

Fig. 7 Sequence showing the evolution of a uniform liquid ridge (covered by a second liquid) on top of a symmetrical junction pattern in a shear cell (see Section 4.1 in the main text for a full description of the initial configuration and the simulation parameters; $\theta_{phil} = 0°$ and $\theta_{phob} = 180°$). The spatial orientation of the system is the same as in Fig. 2(a), *i.e.*, the chemical pattern lies in the xy-plane and the sections are aligned with the x-direction. The surface shown represents snapshots of the interface $\mathscr{A}$ between the two liquids, and the motion is driven by translating the top of the simulation box at a constant velocity $0.3\sigma/t_0$ along the positive x-direction. The frames are labeled by the time in units of t_0. The straight lines indicate the boundaries of the simulation box. For a movie see the file *sheardrivenMD.avi*.

Couette flow) and $\gamma \approx 2.50\varepsilon/\sigma^2$ (found from a standard simulation of a slab of liquid[83]), respectively. Furthermore, we emphasize that MD incorporates thermal fluctuations while (our present version of) LB does not.

Nonetheless, the behavior of the two systems is rather similar. The height of the inner liquid is initially uniform, and some accumulation of water is visible at the nodes of the pattern before the driving force is applied at $t = 50t_0$. The fluids move from left to right (i.e., in the positive x-direction) in response to the top boundary motion, and at $t = 1500t_0$ one pearl of water forms at the upstream node while a second one is traversing the downstream periodic boundary. Due to the symmetry of the wetting pattern, the bulk of the upstream pearl is held in place as additional water arrives through the periodic boundary, while small amounts advance slightly along the circular arcs of the pattern. As in the LB simulations, further symmetric advance along the arcs is impossible due to the finite volume of the liquid available, and water continues to accumulate at the node until $t = 2900t_0$, after which a thermal fluctuation puts more material on the rear arc and the pearl moves along it (see the snapshot at $4100t_0$). Note the extreme overhang of the pearl – only a narrow strip along the arc is actually in contact with the solid. Also, as in the LB figures, the apparently water-free areas are a plotting artifact due to those sampling bins having less than the water density $0.4\sigma^{-3}$ which defines the interface as an isodensity surface. At later times the single pearl reaches and crosses the downstream node as well as the periodic boundary ($5800t_0$), halts temporarily at the upstream node again, and begins to follow the previous path along the rear arc ($7000t_0$). In further repeated traversals of the pattern at later times (not shown), the pearl configuration retains its shape and (approximately) its volume, and always chooses the rear arc of the pattern, because the thicker residue of water left behind there after the first passage provides a less resistive path.

For further illustrations, see the movie file *sheardrivenMD.avi* corresponding to Fig. 8.

4.3 Open flows

Similar simulations have been performed on junction patterns with only one one-component liquid placed on top of the wetting region, leaving the upper parts of the simulation box empty aside from a very dilute vapor resulting from evaporation of the liquid. In Fig. 8 we show the motion of the interface of a liquid–vapor system driven by a pressure gradient. Explicitly, a body force is applied to each fluid atom parallel to the pattern axis, as if the liquid was falling vertically under gravity. However, due to numerical limitations the magnitude of the force had to be chosen to be much larger than terrestrial gravity; a practical experimental procedure corresponding to our simulations might use centrifugal forces on a rotating disk with a radius of 1 cm at 4 $\times 10^4$ rpm.[41] One qualitative change (note the frame at $100t_0$) is that the interface is rougher with much more short length scale variation. This may be understood intuitively as the result of molecules near the surface having greater freedom of movement in the absence of a viscous liquid "cover," and more quantitatively as a consequence of a lower surface tension for the liquid–vapor interface in this simulation ($\gamma = 0.49\varepsilon/\sigma^2$)[39] in comparison to that of the liquid–liquid interface ($\gamma = 2.50\varepsilon/\sigma^2$) considered
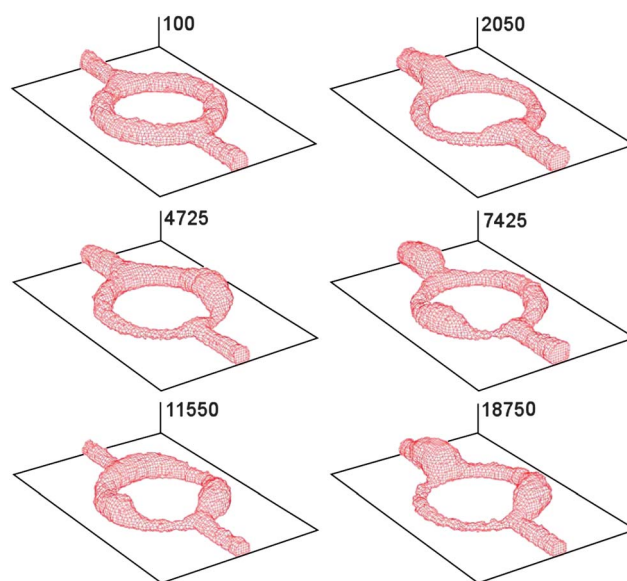

Fig. 8 Sequence showing the evolution of a uniform, one-component liquid ridge on top of a symmetrical wetting pattern in contact with its vapor. The surface represents the liquid–vapor interface $\mathscr{A}$, and motion is driven by a body force of magnitude $0.001m\sigma/t_0^2$. The interaction coefficient $c_{\text{liquid,rock}}$ is 1.0 inside the pattern and 0 outside; $\theta_{\text{phil}} = 0°$ and $\theta_{\text{phob}} = 180°$. The other simulation parameters are given in Section 4.1. For a movie see the file *openflowsmallMD.avi*.

above. A second qualitative difference is that while in the previous simulation there was always a single moving pearl, more diverse morphologies of the interface are seen here. Initially, the fluid motion is similar to the shear-cell case: liquid moves easily through the downstream node and the periodic boundary while accumulating temporarily at the upstream node ($2050t_0$), and then randomly choosing the rear arc to traverse the junction ($4725t_0$). However, on the second traversal, the pearl instead chooses the front arc of the junction ($7425t_0$) because the fluid film being on the front arc after the first traversal through the rear arc happens to be thicker than on the rear arc, perhaps again due to a random fluctuation. At still later times, multiple pearls may be present and in different states of motion. For example at $11\,550t_0$, there are mobile pearls in both arcs and an accumulation at the upstream node of the junction. Subsequently, the bulge at the node merges smoothly into the two pearls which continue to move, following each other repeatedly through the rear arc ($187\,50t_0$). Evidently, the larger fluctuations present in the liquid–vapor case lead to a less regular behavior.

For further details, see the movie file *openflowsmallMD.avi*.

The simulations shown so far have the attractive feature that the water remains on top of the wetting pattern even in motion. But there are limitations to this behavior. In Fig. 9 we report on simulations of a larger system in which the overall size of the simulation box and the "skeleton" of the wetting pattern (i.e., the length of the linear sections and the radius of the centerline of the arcs) are doubled in size, but the width of the wetting channel and the initial height of the liquid are the same as before. This simulation thus involves twice the distance between the nodes and twice the volume of the liquid. As shown, in this case multiple pearls form readily, which may be understood from a
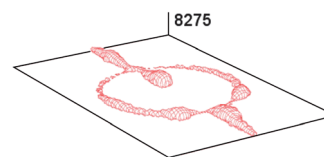
previous analysis of liquid ridges on a linear wetting stripe,[39] which revealed a characteristic critical wavelength for the linear instability leading to pearling behavior. Here, the longer intervals of linear or curved channels exceed this wavelength. A second new feature is that if the liquid is held up at the upstream node (due to symmetry) the additional liquid now present in the system may build up to a pearl too large to be held in place by surface tension forces until a fluctuation breaks the symmetry and an arc of the pattern is selected at random. In this situation, the pearl is simply pulled off the pattern by the driving forces and moves downstream in the vapor. In an alternative simulation, in which the region outside the wetting pattern features partial wetting ($\theta_{\text{phob}} \approx 90°$) rather than nonwetting interactions with the liquid, as shown in Fig. 10 streams of liquid leave the pattern and move straight along the substrate in the direction of the force. More generally, there is a competition between the wetting interactions trying to hold the liquid on the pattern and the applied forcing which attempts to move liquid downstream. If the strength of the forcing or the volume of the liquid which accumulates at a junction is too large, the driving force pushes the liquid along the substrate irrespective of its wetting characteristics.

Further details may be found in the movie files *openflowlargeMD.avi* and *openflowpartialMD.avi* corresponding to Fig. 9 and 10, respectively.

5   Physical units

Our simulation approach aims at reproducing classical fluid dynamic behavior *via* (non-fluctuating) LB and at capturing nano-scale aspects *via* MD. These two methods refer to different length scale regimes. Those regimes are specified by the ratio of the Reynolds and the capillary number,

$$\frac{\text{Re}}{\text{Ca}} = \frac{m\rho\gamma}{(\eta^{\text{w}})^2} w, \qquad (13)$$

which, for given material parameters m, ρ, γ, and η^{w}, implies the value of the channel width w in physical units. Upon taking water under atmospheric pressure and at room temperature as a reference system (*i.e.*, $\gamma \approx 70^{-3}\,\text{kg s}^{-2}$, $\eta^{\text{w}} \approx 10^{-3}\,\text{kg (ms)}^{-1}$, and $m\rho \approx 10^3\,\text{kg m}^{-3}$), the ratios Re/Ca $\approx$ 21.7 for LB and Re/Ca $\approx$ 0.38 for MD (shear-cell flow) imply $w \approx$ 310 nm for LB and $w \approx$ 5.4 nm for MD, and hence, the spatial resolution for LB ($w = 6a$, see Fig. 2(a)) and MD ($w = 17.1\sigma$, see Section 4.1) corresponds to

$$a \approx 51.7\text{ nm} \quad \text{and} \quad \sigma \approx 0.32\text{ nm}, \qquad (14)$$
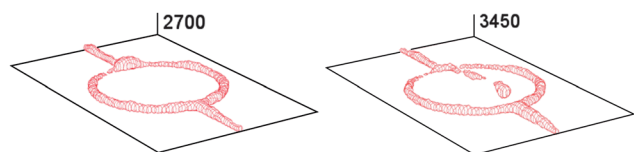

Fig. 9 Behavior of a symmetrical junction pattern with twice the dimensions of Fig. 8. The other simulation parameters are the same as in Fig. 8; $\theta_{\text{phil}} = 0°$ and $\theta_{\text{phob}} = 180°$. Liquid accumulates at the upstream node until its volume is too large to be held on the pattern by surface tension forces and a drop detaches and flies off. For a movie see the file *openflowlargeMD.avi*.

Fig. 10 Fluid behavior on the larger junction pattern of Fig. 9 but with a *partially* wetting exterior ($c_{\text{liquid,rock}} = 0.75$); $\theta_{\text{phil}} = 0°$ and $\theta_{\text{phob}} = 90°$. The other simulation parameters are the same as in Fig. 8. In this case droplets of liquid detach from the pattern and slide along the substrate. For a movie see the file *openflowpartialMD.avi*.

respectively. Likewise, the capillary numbers Ca $\approx$ 0.12 for LB (low shear rate) and Ca $\approx$ 0.56 for MD imply shear velocities $v_{\text{shear}} = \text{Ca}\gamma/\eta^{\text{w}} \approx 8.4\text{ m s}^{-1}$ and $v_{\text{shear}} \approx 39.2\text{m s}^{-1}$, respectively. The intrinsic time scale for our systems, *i.e.*, the typical time scale for thickness undulations of wavelength w on a thin film of this thickness[84] or of a rivulet on a channel of width w is given by[39]

$$t^* = \frac{\eta^{\text{w}}}{\gamma} w = \text{Ca}\,\frac{w}{v_{\text{shear}}}. \qquad (15)$$

Thus one has $t^* \approx$ 4.4 ns for LB and $t^* \approx$ 77 ps for MD. The time resolutions of the LB and MD simulations are (see eqn (2)) $\Delta t = a/(\sqrt{3}c_T) \approx 440$ ps and $t_0 = 0.3\sigma/v_{\text{shear}} \approx 2.4$ ps, respectively.

6   Free energy landscapes

The previous analyses reveal that a key feature of motion through a branched pattern is the behavior of droplets at a node. In order to gain further insight and to elucidate the dynamics associated with this feature, we analyze a simplified quasi-static model which focuses on the effects of surface tension (see Fig. 11 and 12). We consider a non-volatile liquid "water" droplet near a node in contact both with a substrate and a fluid "oil" or vapor phase and perform a minimization of the interfacial free energy $\mathcal{F}$ with respect to the shape $\mathcal{A}$ of the liquid–fluid interface configuration for steplike variations of the contact angle under the constraints of a fixed volume and a fixed lateral position of the center of mass of the droplet (see Fig. 12 and Appendix A). For simplicity we assume the liquid to be confined to the chemical channel, *i.e.*, $\theta_{\text{phob}} = 180°$.

This requires to minimize the functional

$$F = \mathcal{F}[\mathcal{A}] + \Delta p C_p[\mathcal{A}] + \boldsymbol{f}_{\|} \cdot \boldsymbol{C}_{\|}[\mathcal{A}]. \qquad (16)$$

The minimization constraints are encoded in the scalar expression C_P and the vectorial expression $\boldsymbol{C}_{\|} = (C_x, C_y)$ with associated Lagrange multipliers Δp and $\boldsymbol{f}_{\|} = (f_x, f_y)$, respectively.

The constrained minimization is carried out numerically using the surface evolver package.[64] This is an adaptive finite element algorithm, which evolves a certain triangulated, initial interface configuration iteratively towards a state of minimal F via a gradient projection method with Δp, f_x, and f_y as adjustable parameters.

Since the droplet is confined to the chemical channel on which the equilibrium contact angle θ is assumed to be constant the interfacial free energy term in eqn (16) has the form
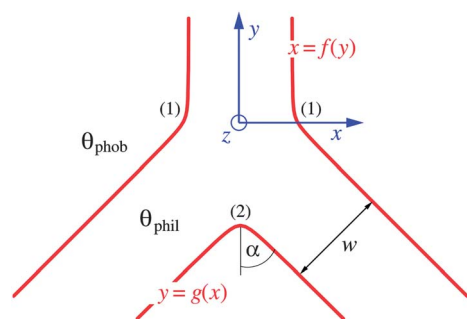
Fig. 11 The chemical pattern given by a Y-shaped (upside down) junction of chemical channels with a uniform width w. The channels are defined by a wettability jump, *i.e.*, a steplike lateral variation of the contact angle $\theta(x,y)$ between hydrophilic and hydrophobic values θ_{phil} and θ_{phob}. The channel edges are given by the expressions $x = f(y) = (b/2)[\sqrt{1 + (y/b)^2} - y/b]\tan\alpha + w/2$ and $y = g(x) = -c\sqrt{1 + (x/c)^2}\tan\alpha - w[1/\sin\alpha - 1/(2\tan\alpha)]$ with the parameters $b = 0.2$ and $c = 0.2$ defining the curvature at the corners (1) and (2), respectively. The red lines indicate $x = \pm f(y)$ and $y = g(x)$, the coordinate axes are drawn in blue, and α is the opening angle of the junction (here $\alpha = 45°$), *i.e.*, the pattern has a yz-mirror symmetry. The origin lies in the mirror-symmetry plane at the position of maximal curvature of the channel edges, *i.e.*, $f''(y = 0) = 0$.
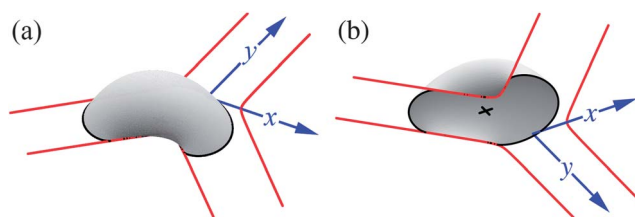

Fig. 12 Top view (a) and bottom view (b) of the interface configuration $\mathscr{A}$ of a non-volatile droplet in the vicinity of the Y-shaped junction of chemical channels shown in Fig. 11, obtained numerically from eqn (16). The three-phase contact line $\mathscr{L}$ bounding $\mathscr{A}$ is drawn in black. The droplet has a volume $V/w^3 = 0.75$, the opening angle is $\alpha = 45°$, $\theta_{\text{phil}} = 60°$, and $\theta_{\text{phob}} = 180°$. The lateral droplet position – indicated by the black cross in (b) – is specified *via* the center of mass projection of $\mathscr{A}$ onto the xy-plane, $\bar{\boldsymbol{r}}_{\|} = (\bar{x}, \bar{y}) = (-0.3w, -0.8w)$.

$$\mathscr{F}[\mathscr{A}] = \gamma \left(\int_{\mathscr{A}} \mathrm{d}A - \cos\theta \oint_{\mathscr{L}} \mathrm{d}\mathbf{l} \cdot \hat{\boldsymbol{n}}_y x \right), \tag{17}$$

with the liquid–fluid interfacial tension γ so that γw^2 provides the scale for the free energy F. The stripe width w (see Fig. 11) is the only lengthscale within this model. Young's contact angle θ measures the wettability of the substrate, and $\hat{\boldsymbol{n}}_y$ is the y-component of the interface normal pointing outwards (see Appendix A). The substrate surface is located in the xy-plane and its tension with the liquid and the fluid contributes *via* an oriented line integral along the boundary of $\mathscr{A}$, *i.e.*, the three-phase contact line $\mathscr{L}$ (Fig. 12). The chemical pattern is given by a steplike lateral variation of the contact angle θ (see Fig. 11 and 12).

Non-volatility is ensured upon constraining the liquid volume to a fixed value V. This constraint is implemented *via* the Lagrange multiplier Δp so that

$$\Delta p C_p = \Delta p (V - \int_{\mathscr{A}} \mathrm{d}A \cdot \hat{\boldsymbol{n}}_z z), \tag{18}$$

where dA is the oriented surface element, and $\hat{\boldsymbol{n}}_z$ is the z-component of the outward normal of the interface. The Lagrange multiplier Δp can be interpreted as the Laplace pressure of the droplet.

The constraint $\boldsymbol{C}_{\|}$ is used in order to fix the center of mass projection of the droplet onto the substrate plane at a certain position $\bar{\boldsymbol{r}}_{\|} = (\bar{x}, \bar{y})$, *i.e.*,

$$\boldsymbol{f}_{\|} \cdot \boldsymbol{C}_{\|} = f_x \left(\bar{x} - \frac{1}{2V} \int_{\mathscr{A}} \mathrm{d}A \cdot \hat{\boldsymbol{n}}_x x^2 \right) + f_y \left(\bar{y} - \frac{1}{2V} \int_{\mathscr{A}} \mathrm{d}A \cdot \hat{\boldsymbol{n}}_y y^2 \right), \tag{19}$$

see Appendix B. The vectorial Lagrange multiplier $\boldsymbol{f}_{\|} = (f_x, f_y)$ can be interpreted as a spatially constant, lateral force field, which suitably balances the effect of surface tension forces. In other words, the configurational space $\{\mathscr{A}\}$ for the minimization of the free energy functional $\mathscr{F}[\mathscr{A}]$, which has been restricted to a subspace of interface shapes with a certain volume V by the constraint C_p given in eqn (18), is restricted further to the subspace of shapes with a certain center of mass projection $\bar{\boldsymbol{r}}_{\|}$. Naturally, this method only works for droplets with a finite support, *i.e.*, for $\theta_{\text{phil}} > 0°$.

With this, the free energy F of a droplet on the pattern can be obtained as a function of $\bar{x}$ and $\bar{y}$ with V and the wettability contrast $\theta_{\text{phob}} - \theta_{\text{phil}}$ as input parameters (see Fig. 13 for the topography and a corresponding contour plot of $F(\bar{x}, \bar{y})$). Naturally, the chemical channels translate into energetic valleys with a global minimum at $(\bar{x} = 0, \bar{y} \approx -0.4w)$ near the intersection point of the channel midlines at $\bar{y} = \frac{w}{2}(1 - (\sin 45°)^{-1}) \approx -0.2w$. Upon decreasing the wettability contrast the topography of the free energy landscape becomes less structured: the depth of the global minimum relative to the free energy of a droplet far from the chemical channels as well as relative to the free energy of a droplet on a straight channel decreases (see Fig. 14(a) and (b), respectively). However, the position of the global minimum does not shift (see Fig. 14(b)). The $\bar{y}$-position of the minimum certainly depends on the opening angle α. For $\alpha = 60°$, *i.e.*, for a threefold rotational symmetry of the junction, it is right at the intersection point of the channel midlines.

The occurrence of the global free energy minimum at the pattern junction implies a certain qualitative behavior of the droplet: an unconstrained droplet – given by $\boldsymbol{f}_{\|} \equiv 0$ within eqn (16) – would be sucked in and trapped at the junction. Equivalently, a trapped droplet has to overcome a free energy barrier in order to escape from the junction. In this respect it is worthwhile to compare this with the LB-results in Fig. 4–6, which show preferential droplet formation on the junction during pearling, as well as the hang-up and merger of driven droplets there. In particular Fig. 6(a) shows a permanent hang-up for $\theta_{\text{phil}} \approx 30°$.

The contour plot in Fig. 13(b) shows that the consequences of the free energy minimum, *i.e.*, leading to a possible droplet hang-up, can be avoided by guiding the droplet *via* an additional external, lateral force in such a way that its center of mass projection $\bar{\boldsymbol{r}}_{\|}$ moves along an open contour line.
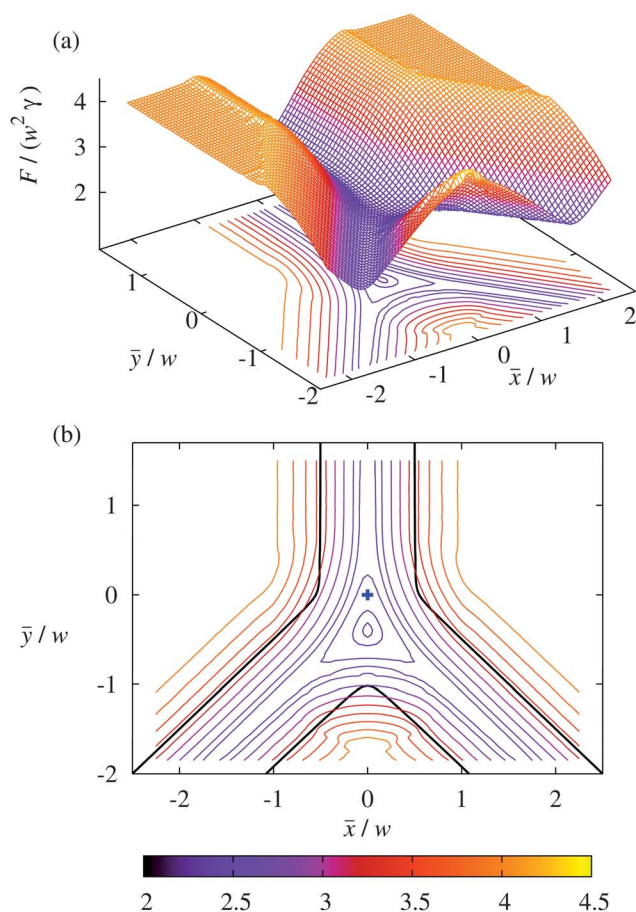
Fig. 13 The topography (a) and the corresponding contour plot (b) of the free energy $F(\bar{x}, \bar{y})$ as a function of the center of mass coordinates $\bar{x}$ and $\bar{y}$ in the xy-plane for the system shown in Fig. 12. The blue cross within the contour plot indicates the origin of the coordinate system (see Fig. 11) and the black lines correspond to the positions of the channel boundaries (see Fig. 11). There is a minimum of F at ($\bar{x} = 0, \bar{y} \approx -0.4w$).
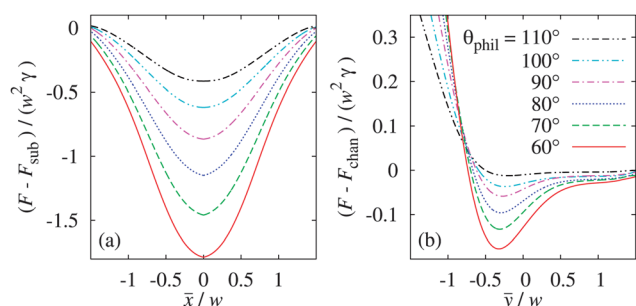

Fig. 14 Cuts of the free energy landscapes for $V/w^3 = 0.75$, $\alpha = 45°$, $\theta_{\text{phob}} = 180°$, and various hydrophilic contact angles $\theta_{\text{phil}} \in [60°, 110°]$, (a) along $\bar{x}$ through the global minimum and (b) along the $\bar{y}\bar{z}$-symmetry plane at $\bar{x} = 0$. Due to the symmetry of the system the global minimum always occurs at $\bar{x} = 0$. In (a) and (b) the free energy is shown relative to the free energy of a droplet on a homogeneous hydrophobic substrate $F_{\text{sub}} = F(\bar{x} \to \pm\infty, \bar{y})$ and on a homogeneous straight chemical channel $F_{\text{chan}} = F(|\bar{x}| < w, \bar{y} \to \infty)$, respectively. Therefore the values for the depths of the minima in (a) and (b) differ.

7 Summary, conclusion, and outlook

We have analyzed theoretically the forced motion of liquid rivulets through branched chemical patterns on a substrate (Fig. 2 and 3). The purpose of this study is to demonstrate the feasibility of this set-up for controlled fluid transport, which might serve as a component of future "lab-on-a-chip" devices. Our calculations employ a lattice Boltzmann method (Fig. 1) for the isothermal description of microscale systems and molecular dynamics for their nanoscale counterparts.

The microscale simulations (see Fig. 4–6) show that within reasonable limitations for the flow rate and the liquid volume, the wetting pattern is capable of directing liquid motion along desired paths. Familiar surface tension instabilities lead to pearl formation at the nodes of the pattern (see in particular Fig. 4), but as in simpler flow configurations [39,41] the pearls are mobile and move along the pattern, and therefore need not to obstruct the motion of the liquid. Although the nanoscale systems are particularly sensitive to thermal fluctuations, the behavior of the liquid in this domain is nonetheless fairly similar (see Fig. 7–10).

Concerning the possibility to control these systems the challenge is to direct the liquid preferentially along one of the multiple paths leaving a node. Our microscale simulations indicate that small variations in the width of the wetting channels can suffice for this purpose (see Fig. 5(b) and 6(b)). The liquid prefers to move along a wider channel where viscous resistance is lower. Other mechanisms for directing flow, such as imposed electric fields acting on an ionic liquid, bursts of air directed towards one side of a node, smooth wettability gradients on the surface, *etc.*, might work as well or better. We leave these possibilities for future studies.

For a qualitative understanding of the behavior of driven pearls at the nodes we have employed a quasi-static model based on the action of surface tensions. This yields the free energy landscape with a state of minimal free energy for an isolated droplet sitting at a node (see Fig. 11–14).

Likewise, an additional consideration for future work is the behavior of suspensions or complex liquids, *e.g.*, lyotropic or thermotropic liquid crystals, flowing along chemical patterns.

A Free energy

Using the local version of Young's law, $\gamma\cos\theta(x,y) = \gamma_{\text{rf}}(x,y) - \gamma_{\text{rw}}(x,y)$ with the indices r, w, and f for "rock", "water", and "fluid" (*i.e.*, "oil" or vapor), respectively, within the capillary model for a chemically heterogeneous substrate domain with a laterally varying macroscopic contact angle $\theta(x,y)$ the free energy $\mathscr{F}$ can be expressed as

$$\frac{\mathscr{F}}{\gamma} = \int_{\mathscr{A}} dA - \int_{\mathscr{S}} dA \cdot \hat{\boldsymbol{n}}_z \cos\theta(x,y) \qquad (20)$$

with the liquid–fluid interfacial tension γ as a scaling parameter. Here we assume that the substrate surface and thus also the "water"–substrate interface $\mathscr{S}$ lie in the xy-plane and that $\mathscr{S}$ is oriented such that its normal vector is $\hat{\boldsymbol{n}}_z = (0,0,1)$.

The integral over $\mathscr{S}$ can be converted into an integral over the three-phase contact line if one finds a vector potential for the vector field $\hat{\boldsymbol{n}}_z \cos\theta(x,y)$. A simple (and for the present geometry convenient) choice of the corresponding gauge is adopted by

$$\hat{n}_z \cos\theta(x,y) = \nabla \times [\hat{n}_y C(x,y)], \qquad (21)$$

with $\hat{n}_y = (0,1,0)$ and $C(x,y) = \int_{x_0}^{x} dx' \cos\theta(x',y)$. (Note that $\nabla \times [\hat{n}_y C(x,y)]$ is independent of x_0.) Applying Stokes' theorem yields

$$\frac{\mathscr{F}[\mathscr{A}]}{\gamma} = \int_{\mathscr{A}} dA - \oint_{\mathscr{L}} d\boldsymbol{l} \cdot \hat{n}_y C(x,y), \qquad (22)$$

where the three-phase contact line $\mathscr{L}$ is the oriented boundary of $\mathscr{S}$ as well as of $\mathscr{A}$ (see Fig. 12).

If a chemical pattern with a steplike variation of the local equilibrium contact angle $\theta(x,y)$ confines the drop to a chemically homogeneous part of the substrate eqn (22) reduces to eqn (17). This holds even if a portion of $\mathscr{L}$ coincides with an interval of the boundary of the chemical channel.

B Center of mass constraint

In order to constrain the lateral position of the center of mass $V^{-1} \int_V dV \boldsymbol{r}$ of a droplet of volume V and of homogeneous density to $(\bar{x}, \bar{y})$ one adds the expression

$$\boldsymbol{f}_{\parallel} \cdot \boldsymbol{C}_{\parallel} = f_x \left(\bar{x} - \frac{1}{V} \int_V dV x \right) + f_y \left(\bar{y} - \frac{1}{V} \int_V dV y \right) \qquad (23)$$

with the Lagrange multiplier $\boldsymbol{f}_{\parallel} = (f_x, f_y)$ to the free energy functional. The volume integrals in eqn (23) can be converted into surface integrals using Gauß' theorem. To this end one expresses each of the scalar integrands as the divergence of a suitable vector field. For droplets residing on a planar substrate which lies in the xy-plane a convenient choice is

$$x = \nabla \cdot \left(\frac{1}{2} x^2 \hat{n}_x \right) \text{ and } y = \nabla \cdot \left(\frac{1}{2} y^2 \hat{n}_y \right). \qquad (24)$$

Since the area element $d\boldsymbol{S} = dS \hat{n}_z$ of $\mathscr{S}$ is orthogonal to $\hat{n}_x$ and $\hat{n}_y$ the contribution of the surface integral over the liquid–substrate interface $\mathscr{S}$ to the surface integral over the total surface of V vanishes and the term $\boldsymbol{f}_{\parallel} \cdot \boldsymbol{C}_{\parallel}$ in eqn (16) reduces to the expression given in eqn (19).

Acknowledgements

References

1 P. Mitchell, *Nat. Biotechnol.*, 2001, **19**, 717–721.
2 T. Thorsen, S. J. Maerkl and S. R. Quake, *Science*, 2002, **298**, 580–584.
3 H. A. Stone, A. D. Strook and A. Ajdari, *Annu. Rev. Fluid Mech.*, 2004, **36**, 381–411.
4 T. M. Squires and S. R. Quake, *Rev. Mod. Phys.*, 2005, **77**, 977–1026.
5 D. Mark, S. Haeberle, G. Roth, F. von Stetten and R. Zengerle, *Chem. Soc. Rev.*, 2010, **39**, 1153–1182.
6 P. Abgrall and N. T. Nguyen, *Anal. Chem.*, 2008, **80**, 2326–2341.
7 A. van den Berg, H. G. Craighead and P. Yang, *Chem. Soc. Rev.*, 2010, **39**, 899–900.
8 Y. Imry, *Introduction to Mesoscopic Physics*, Oxford University Press, New York, 1997.
9 V. T. A. Tagliacozzo and B. L. Altshuler, *Quantum Phenomena in Mesoscopic Systems (International School of Physics Enrico Fermi)*, IOS Press, New York, 2003.
10 T. Heinzel, *Mesoscopic Electronics in Solid State Nanostructures*, Wiley-VCH, Weinheim, 2007.
11 J. C. T. Eijkel and A. van den Berg, *Microfluid. Nanofluid.*, 2005, **1**, 249–267.
12 R. Mukhopadhyay, *Anal. Chem.*, 2006, **78**, 7379–7382.
13 R. B. Schoch, J. Han and P. Renaud, *Rev. Mod. Phys.*, 2008, **80**, 839–883.
14 M. L. Kovarik and S. C. Jacobson, *Anal. Chem.*, 2009, **81**, 7133–7140.
15 L. Bocquet and E. Charlaix, *Chem. Soc. Rev.*, 2010, **39**, 1073–1095.
16 R. Roth and D. Gillespie, *Phys. Rev. Lett.*, 2005, **95**, 247801.
17 R. Roth and M. Kroll, *J. Phys.: Condens. Matter*, 2006, **18**, 6517–6530.
18 B. Husowitz and V. Talanquer, *J. Chem. Phys.*, 2007, **126**, 224703.
19 R. Roth, D. Gillespie, W. Nonner and R. E. Eisenberg, *Biophys. J.*, 2008, **94**, 4282–4298.
20 R. Roth, M. Rauscher and A. J. Archer, *Phys. Rev. E: Stat., Nonlinear, Soft Matter Phys.*, 2009, **80**, 021409.
21 N. Schwierz and P. Nielaba, *Phys. Rev. E: Stat., Nonlinear, Soft Matter Phys.*, 2010, **82**, 031401.
22 S. Buyukdagli, M. Manghi and J. Palmeri, *Phys. Rev. Lett.*, 2010, **105**, 158103.
23 A. González, J. A. White, F. L. Romn and S. Velasco, *J. Chem. Phys.*, 2011, **135**, 154704.
24 H. Gau, S. Herminghaus, P. Lenz and R. Lipowsky, *Science*, 1999, **283**, 46–49.
25 S. Dietrich, M. N. Popescu and M. Rauscher, *J. Phys.: Condens. Matter*, 2005, **17**, S577–S593.
26 A. A. Darhuber and S. M. Troian, *Annu. Rev. Fluid Mech.*, 2005, **37**, 425–455.
27 M. Rauscher and S. Dietrich, *Annu. Rev. Mater. Res.*, 2008, **38**, 143–172.
28 J. W. van Honschoten, N. Brunets and N. R. Tas, *Chem. Soc. Rev.*, 2010, **39**, 1096–1114.
29 M. K. Chaudhury and G. M. Whitesides, *Science*, 1992, **256**, 1539–1541.
30 C. Quilliet and B. Berge, *Curr. Opin. Colloid Interface Sci.*, 2001, **6**, 34–39.
31 J. Zeng and T. Korsmeyer, *Lab Chip*, 2004, **4**, 265–277.
32 V. Srinivasan, V. K. Pamula and R. B. Fair, *Lab Chip*, 2004, **4**, 310–315.
33 F. Mugele and J.-C. Baret, *J. Phys.: Condens. Matter*, 2005, **17**, R705–R774.
34 P. Siribunbandal, S. Yamaguchi, K. Kojima, J. Fukuda and H. Suzuki, *Appl. Phys. Lett.*, 2009, **95**, 204105.
35 N. Garnier, R. O. Grigoriev and M. F. Schatz, *Phys. Rev. Lett.*, 2003, **91**, 054501.
36 K. T. Kotz, K. A. Noble and G. W. Faris, *Appl. Phys. Lett.*, 2004, **85**, 2658–2660.
37 M. A. Burns, C. H. Mastrangelo, T. S. Sammarco, F. P. Man, J. R. Webster, B. N. Johnsons, B. Foerster, D. Jones, Y. Fields, A. R. Kaiser and D. T. Burke, *Proc. Natl. Acad. Sci. U. S. A.*, 1996, **93**, 5556–5561.
38 R. H. Farahi, A. Passian, T. L. Ferrell and T. Thundat, *Appl. Phys. Lett.*, 2004, **85**, 4237–4239.
39 J. Koplik, T. S. Lo, M. Rauscher and S. Dietrich, *Phys. Fluids*, 2006, **18**, 032104.
40 Z. Guttenberg, H. Müller, H. Habermüller, A. Geisbauer, J. Pipper, J. Felbel, M. Kielpinski, J. Scriba and A. Wixforth, *Lab Chip*, 2005, **5**, 308–317.
41 M. Rauscher, S. Dietrich and J. Koplik, *Phys. Rev. Lett.*, 2007, **98**, 224504.
42 R. Lipowsky, P. Lenz and P. S. Swain, *Colloids Surf., A*, 2000, **161**, 3–22.
43 R. Lipowsky, *Curr. Opin. Colloid Interface Sci.*, 2001, **6**, 40–48.
44 M. Brinkmann and R. Lipowsky, *J. Appl. Phys.*, 2002, **92**, 4296–4306.
45 R. Lipowsky, M. Brinkmann, R. Dimova, C. Haluska, J. Kierfeld and J. Shillcock, *J. Phys.: Condens. Matter*, 2005, **17**, S2885–S2902.
46 P. Lenz, W. Fenzl and R. Lipowsky, *Europhys. Lett.*, 2001, **53**, 618–624.
47 F. Porcheron, P. A. Monson and M. Schoen, *Phys. Rev. E: Stat., Nonlinear, Soft Matter Phys.*, 2006, **73**, 041603.
48 P. G. de Gennes, *Rev. Mod. Phys.*, 1985, **57**, 827–860.

49 S. Dietrich, in *Phase Transitions and Critical Phenomena*, ed. C. Domb and J. L. Lebowitz, Academic, London, 1988, vol. 12, pp. 1–218.

50 C. Bauer and S. Dietrich, *Phys. Rev. E: Stat. Phys., Plasmas, Fluids, Relat. Interdiscip. Top.*, 1999, **60**, 6919–6941.

51 C. Bauer and S. Dietrich, *Eur. Phys. J. B*, 1999, **10**, 767–779.

52 C. Bauer, S. Dietrich and A. O. Parry, *Europhys. Lett.*, 1999, **47**, 474–480.

53 C. Bauer and S. Dietrich, *Phys. Rev. E: Stat. Phys., Plasmas, Fluids, Relat. Interdiscip. Top.*, 2000, **61**, 1664–1669.

54 A. Checco, O. Gang and B. M. Ocko, *Phys. Rev. Lett.*, 2006, **96**, 056104.

55 A. Checco, *Phys. Rev. Lett.*, 2009, **102**, 106103.

56 R. Blossey, *Phys. Chem. Chem. Phys.*, 2008, **10**, 5177–5183.

57 J. De Coninck and T. D. Blake, *Annu. Rev. Mater. Res.*, 2008, **38**, 1–22.

58 J. Ralston, M. Popescu and R. Sedev, *Annu. Rev. Mater. Res.*, 2008, **38**, 23–43.

59 D. Quéré, *Annu. Rev. Mater. Res.*, 2008, **38**, 71–99.

60 S. Herminghaus, M. Brinkmann and R. Seemann, *Annu. Rev. Mater. Res.*, 2008, **38**, 101–121.

61 R. V. Craster and O. K. Matar, *Rev. Mod. Phys.*, 2009, **81**, 1131–1198.

62 K. F. McCarty, J. C. Hamilton, Y. Sato, A. Saá, R. Stumpf, J. de la Figuera, K. Thürmer, F. Jones, A. K. Schmid, A. A. Talin and N. C. Bartelt, *New J. Phys.*, 2009, **11**, 043001.

63 D. Frenkel and B. Smit, *Understanding Molecular Simulation*, Academic, San Diego, 2nd edn, 2002.

64 K. Brakke, *Exp. Math.*, 1992, **1**, 141–165.

65 X. Shan and H. Chen, *Phys. Rev. E: Stat. Phys., Plasmas, Fluids, Relat. Interdiscip. Top.*, 1993, **47**, 1815–1819.

66 X. Shan and H. Chen, *Phys. Rev. E: Stat. Phys., Plasmas, Fluids, Relat. Interdiscip. Top.*, 1994, **49**, 2941–2948.

67 X. Shan and G. Doolen, *J. Stat. Phys.*, 1995, **81**, 379–393.

68 M. R. Swift, W. R. Osborn and J. M. Yeomans, *Phys. Rev. Lett.*, 1995, **75**, 830–833.

69 M. R. Swift, E. Orlandini, W. R. Osborn and J. M. Yeomans, *Phys. Rev. E: Stat. Phys., Plasmas, Fluids, Relat. Interdiscip. Top.*, 1996, **54**, 5041–5052.

70 A. K. Gunstensen, D. H. Rothman, S. Zaleski and G. Zanetti, *Phys. Rev. A: At., Mol., Opt. Phys.*, 1991, **43**, 4320–4327.

71 S. V. Lishchuk, C. M. Care and I. Halliday, *Phys. Rev. E: Stat. Phys., Plasmas, Fluids, Relat. Interdiscip. Top.*, 2003, **67**, 036701.

72 H. Kusumaatmaja, J. Léopoldès, A. Dupuis and J. M. Yeomans, *Europhys. Lett.*, 2006, **73**, 740–746.

73 H. Kusumaatmaja and J. Yeomans, *Langmuir*, 2007, **23**, 956–959.

74 M. Nekovee, P. V. Coveney, H. Chen and B. M. Boghosian, *Phys. Rev. E: Stat. Phys., Plasmas, Fluids, Relat. Interdiscip. Top.*, 2000, **62**, 8282–8294.

75 J. Harting, J. Chin, M. Venturoli and P. V. Coveney, *Philos. Trans. R. Soc. London, Ser. A*, 2005, **363**, 1895–1915.

76 Z. Guo, C. Zheng and B. Shi, *Phys. Rev. E: Stat. Phys., Plasmas, Fluids, Relat. Interdiscip. Top.*, 2002, **65**, 046308.

77 F. Jansen and J. Harting, *Phys. Rev. E: Stat., Nonlinear, Soft Matter Phys.*, 2011, **83**, 046707.

78 Y. H. Qian, D. D'Humières and P. Lallemand, *Europhys. Lett.*, 1992, **17**, 479–484.

79 S. Chen and G. D. Doolen, *Annu. Rev. Fluid Mech.*, 1998, **30**, 329–364.

80 L.-S. Luo, *Phys. Rev. E: Stat. Phys., Plasmas, Fluids, Relat. Interdiscip. Top.*, 2000, **62**, 4982–4996.

81 H. Chen, S. Chen and W. H. Matthaeus, *Phys. Rev. A: At., Mol., Opt. Phys.*, 1992, **45**, R5339–R5342.

82 S. Schmieschek and J. Harting, *Comm. Comput. Phys.*, 2011, **9**, 1165–1178.

83 J. S. Rowlinson and B. Widom, *Molecular Theory of Capillarity*, Dover, Mineola, NY, 2002.

84 A. M. Willis and J. B. Freund, *Phys. Fluids*, 2010, **22**, 022002.